

Experimental evaluation of thermodynamic cost and speed limit in living cells via information geometry

Keita Ashida

The University of Tokyo

Kazuhiro Aoki

National Institutes of Natural Sciences, National Institute for Basic Biology <https://orcid.org/0000-0001-7263-1555>

Sosuke Ito (✉ sosuke.ito@ubi.s.u-tokyo.ac.jp)

The University of Tokyo <https://orcid.org/0000-0001-6954-1321>

Physical Sciences - Article

Keywords: Chemical Reaction Information Processing, Stochastic Thermodynamics, Information-geometric Method, Thermodynamic Uncertainty Relations, Signal Transduction Pathways

Posted Date: December 9th, 2020

DOI: <https://doi.org/10.21203/rs.3.rs-118501/v1>

License: © ⓘ This work is licensed under a Creative Commons Attribution 4.0 International License.

[Read Full License](#)

Experimental evaluation of thermodynamic cost and speed limit in living cells via information geometry

Keita Ashida,¹ Kazuhiro Aoki,^{2,3,4} and Sosuke Ito^{1,5,6}

¹*Universal Biology Institute, The University of Tokyo, 7-3-1 Hongo, Bunkyo-ku, Tokyo 113-0033, Japan*

²*Quantitative Biology Research Group, Exploratory Research Center on Life and Living Systems (ExCELLS), National Institutes of Natural Sciences, 5-1 Higashiyama, Myodaiji-cho, Okazaki, Aichi 444-8787, Japan*

³*Division of Quantitative Biology, National Institute for Basic Biology, National Institutes of Natural Sciences, 5-1 Higashiyama, Myodaiji-cho, Okazaki, Aichi 444-8787, Japan*

⁴*Department of Basic Biology, School of Life Science,*

SOKENDAI (The Graduate University for Advanced Studies),

5-1 Higashiyama, Myodaiji-cho, Okazaki, Aichi 444-8787, Japan

⁵*Department of Physics, The University of Tokyo, 7-3-1 Hongo, Bunkyo-ku, Tokyo 113-0033, Japan*

⁶*JST, PRESTO, 4-1-8 Honcho, Kawaguchi, Saitama, 332-0012, Japan*

Chemical reactions are responsible for information processing in living cells, and their accuracy and speed have been discussed from a thermodynamic viewpoint [1–5]. The recent development in stochastic thermodynamics enables evaluating the thermodynamic cost of information processing [6–8]. However, because experimental estimation of the thermodynamic cost based on stochastic thermodynamics requires a sufficient number of samples [9], it is only estimated in simple living systems, such as RNA folding [10] and F₁-ATPase [11]. Therefore, it is challenging to estimate the thermodynamic cost of information processing by chemical reactions in living cells. Here, we evaluated the thermodynamic cost and its efficiency of information processing in living systems at the single-cell level for the first time by establishing an information-geometric method to estimate them with a relatively small number of samples. We evaluated the thermodynamic cost of the extracellular signal-regulated kinase (ERK) phosphorylation from the time series of the fluorescence imaging data by calculating the intrinsic speed in information geometry. We also evaluated a thermodynamic efficiency based on the thermodynamic speed limit [8, 12, 13], and thus this paper reports the first experimental test of thermodynamic uncertainty relations in living systems. Our evaluation revealed the change of the efficiency under the conditions of different cell densities and its robustness to the upstream pathway perturbation. Because our approach is widely applicable to other signal transduction pathways, such as the G-protein coupled receptor pathways for sensation [14], it would clarify efficient mechanisms of information processing in such a living system.

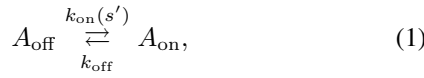
The Gibbs free energy change mainly drives information transmission in living cells, and its mechanism follows thermodynamic laws. For example, systems biology reveals a deep connection between information transmission accuracy and the Gibbs free energy change in a cell [1, 2]. In recent developments of stochastic thermodynamics [15] and chemical thermodynamics [16, 17], a similar connection occurs more deeply. The trade-off relations among speed, thermodynamic cost, and accuracy in a living cell have been proposed [3, 4], and its general thermodynamic bound of information processing in signal transduction has been discussed

in terms of Maxwell’s demon [5, 18–20]. Moreover, as thermodynamic generalizations of uncertainty relations, thermodynamic trade-off relations have been intensively studied in terms of thermodynamic uncertainty relations [21, 22] and thermodynamic speed limits [8, 23–29]. These trade-off relations are mainly based on mathematical properties of the Fisher information [8, 12, 30], which gives a metric of information geometry [31]. Historically, information geometry has been considered as a possible choice of differential geometry for equilibrium thermodynamics [7, 32]. In recent years, information geometry meets nonequilibrium thermodynamics such as stochastic thermodynamics [8, 12, 33] and chemical thermodynamics [13], and it provides a unified framework to derive these trade-off relations in living systems [8, 12, 13]. While theoretical progress of thermodynamic trade-off relations has been intensively made for biological applications, the thermodynamic uncertainty relation has been experimentally tested only in artificial systems [34, 35]. An experimental test of thermodynamic trade-off relations in living systems has not been reported, and the thermodynamic speed limit has not been tested even in artificial systems.

This paper experimentally evaluated the thermodynamic cost by quantifying the Fisher information of time from the fluorescence imaging of the ERK phosphorylation in normal rat kidney epithelial (NRK-52E) cells. In information geometry, the Fisher information of time is regarded as the square of the intrinsic speed. This Fisher information is calculated from the time evolution of the phosphorylated ERK fraction, which can be experimentally measured by the Förster resonance energy transfer (FRET) signal. We also evaluated other information-geometric quantities for activation and inactivation processes from this Fisher information, and these information-geometric quantities illustrate the thermodynamic cost of the ERK phosphorylation, which is related to the Gibbs free energy change and the fluctuation-response ratio. We focused on the thermodynamic speed limit based on these information-geometric quantities and found that the efficiency ranges from 0.4 to 0.9 for the ERK phosphorylation in living NRK-52E cells. We quantified the thermodynamic variability for cell density changes and the perturbation of the upstream Raf pathway. While the cell density increases the thermodynamic cost and reduces efficiency, the Raf inhibitor

addition reduces the thermodynamic cost, but the efficiency is robust to the Raf inhibitor addition.

The information-geometric method proposed in this paper is generally applicable to switching dynamics between the active state and the inactive state. We consider the following chemical reaction



where A_{on} is an active state, A_{off} is an inactive state, s' is stimulus, and $k_{\text{on}}(s')$ and k_{off} are rate constants. Because $k_{\text{on}}(s')$ can depend on stimulus s' , it causes a pulsatile response of A_{on} if this stimulus s' is excitable. This paper focuses on the ERK phosphorylation in the Ras-Raf-MEK-ERK pathway that shows a pulsatile response [36–38]. In Fig. 1a, we show the Ras-Raf-MEK-ERK pathway that relays extracellular stimuli such as growth factors from the plasma membrane to targets in the cytoplasm and nucleus. This three-tiered Raf-MEK-ERK mitogen-activated protein kinase (MAPK) cascade plays an essential role in various cellular processes, including cell proliferation, differentiation, and tumorigenesis [39]. Upon growth factor stimulation, the receptor tyrosine kinase (RTK) activates the Ras small GTPase at the plasma membrane, which recruits and activates the Raf. The activated Raf induces activation and phosphorylation of the MEK. The upstream kinase MEK phosphorylates the ERK to increase kinase activation of the ERK. The phosphorylated ERK is finally dephosphorylated by phosphatases, thereby shutting down the ERK activation. The phosphorylated MEK catalyzes a phosphate transfer from the adenosine triphosphate (ATP) to the ERK, and the Gibbs free energy difference of ATP hydrolysis thermodynamically drives this phosphorylation of the ERK [39, 40]. Here, A_{on} corresponds to a phosphorylated state of the ERK, A_{off} corresponds to a nonphosphorylated state of the ERK, and s' corresponds to the stimulus by upstream proteins in the Ras-Raf-MEK-ERK pathway, respectively. We try to estimate the thermodynamic cost of the ERK phosphorylation in living cells using the time series of the phosphorylated ERK fraction, which can be experimentally measured by the FRET technique at the single-cell level [37].

We discuss the thermodynamic cost estimation from the time series of the phosphorylated ERK fraction $P_1 = [A_{\text{on}}]/([A_{\text{on}}] + [A_{\text{off}}])$, where $[A_{\text{on}}]$ and $[A_{\text{off}}]$ are concentrations corresponding to A_{on} and A_{off} , respectively (see also Supplementary Note). In general, it is hard to estimate the Gibbs free energy change in living cells because it needs prior knowledge about the equilibrium concentration [16]. However, this equilibrium concentration is not estimated well from the time series of P_1 . We propose a novel information-geometric method to estimate the thermodynamic cost from P_1 , which does not require prior knowledge about the equilibrium concentration. Because the total concentration $[A_{\text{tot}}] = [A_{\text{off}}] + [A_{\text{on}}]$ is conserved, the nonphosphorylated and phosphorylated ERK fractions $P_0 = 1 - P_1 = [A_{\text{off}}]/[A_{\text{tot}}]$ and $P_1 = [A_{\text{on}}]/[A_{\text{tot}}]$ can be regarded as the probability distribution, and a Riemannian manifold can be introduced as the set of probability distributions in information geometry [31].

This method focuses on an intrinsic speed $ds/dt = \sqrt{ds^2/dt^2}$ on this manifold related to the thermodynamic cost, such as the Gibbs free energy change and the fluctuation-response ratio of the ERK phosphorylation [8, 12, 13]. The square of the intrinsic speed is given by the Fisher information of time

$$\frac{ds^2}{dt^2} = \sum_{i=0}^1 P_i \left(\frac{d \ln P_i}{dt} \right)^2 = \sum_{i=0}^1 \frac{1}{P_i} \left(\frac{dP_i}{dt} \right)^2. \quad (2)$$

Because ds^2/dt^2 only consists of the concentration fraction P_i and its change speed dP_i/dt , we can estimate it from the time series of P_1 .

The square of the intrinsic speed can quantify the thermodynamic cost of ERK phosphorylation (see also Supplementary Note). Under near-equilibrium condition, we obtain $ds^2/dt^2 \simeq -(d\sigma/dt)/(2R[A_{\text{tot}}])$, where R is the gas constant, and σ is the entropy production that is the minus sign of the Gibbs free energy change over the temperature [13]. Then, the Fisher information of time is proportional to the entropy production rate change under near-equilibrium condition. Even for a system far from equilibrium, the square of the intrinsic speed gives the fluctuation-response ratio of the ERK phosphorylation. Let f_i be an observable of the ERK states, where $i = 0 (i = 1)$ means the nonphosphorylated (phosphorylated) state. The square of the intrinsic speed ds^2/dt^2 is equal to the fluctuation-response ratio

$$\frac{ds^2}{dt^2} = \frac{|d_t \langle f \rangle_t|^2}{\text{Var}[f]_t}, \quad (3)$$

where $\langle f \rangle_t = \sum_i P_i(t) f_i$ is the mean value, $|d_t \langle f \rangle_t| = |d \langle f \rangle_t / dt|$ implies the time-response of the observable, and $\text{Var}[f]_t = \langle f^2 \rangle_t - \langle f \rangle_t^2$ implies the observable fluctuation. This relation is a consequence of the Cramér-Rao inequality for an efficient estimator, where any observable of a binary state can be regarded as an efficient estimator.

As shown in Fig. 1b, a pulsatile response consists of activation and inactivation processes, and we introduce information-geometric quantities of these processes as measures of the thermodynamic cost and the speed limit's efficiency (see also Supplementary Note). During the activation (inactivation) process, the phosphorylated ERK fraction P_1 is monotonically increasing (decreasing) in time. The activation (inactivation) starts at time $t_0 = t_{\text{ini}}$ ($t_0 = t_{\text{peak}}$) and ends at time $t_1 = t_{\text{peak}}$ ($t_1 = t_{\text{fin}}$). We here introduce three information-geometric quantities [7, 8], the action

$$C = \frac{1}{2} \int_{t_0}^{t_1} dt \frac{ds^2}{dt^2}, \quad (4)$$

the length

$$\mathcal{L} = \int_{t_0}^{t_1} \sqrt{\frac{ds^2}{dt^2}} dt = 2 \arccos \left[\sum_{i=0}^1 \sqrt{P_i|_{t=t_0} P_i|_{t=t_1}} \right], \quad (5)$$

and the mean velocity

$$\mathcal{V} = \frac{\mathcal{L}}{t_1 - t_0}, \quad (6)$$

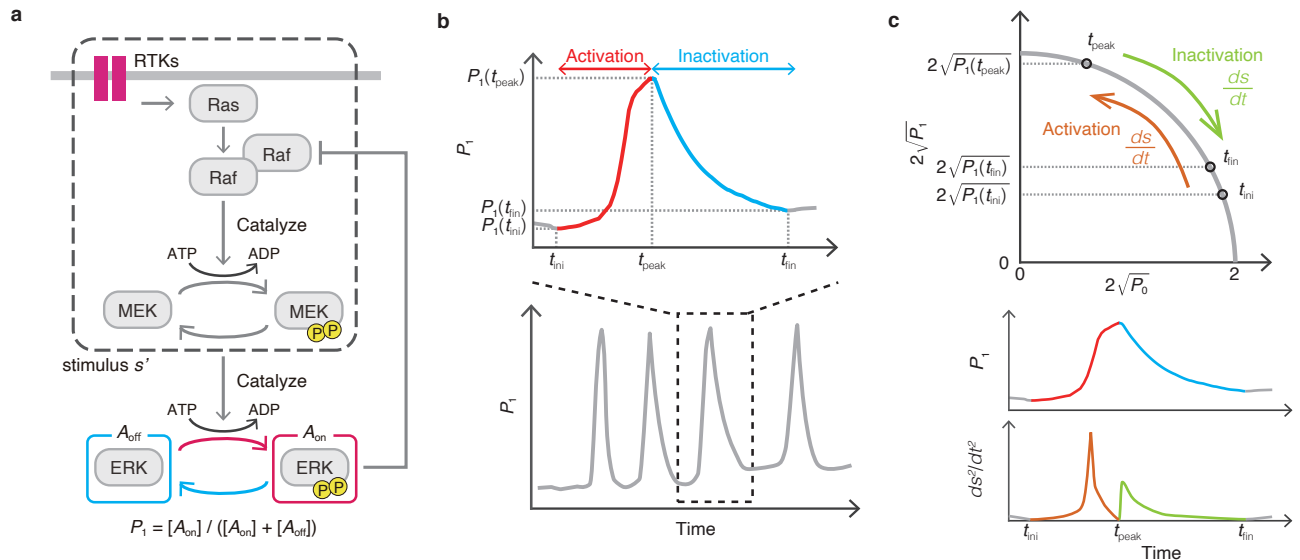


Fig. 1: Schematic of the ERK phosphorylation, the time series of the phosphorylated ERK fraction P_1 , and the square of the intrinsic speed ds^2/dt^2 . **a** The Raf-MEK-ERK MAP pathway as an example of switching dynamics between the active state A_{on} and the inactive state A_{off} . The phosphorylated and nonphosphorylated ERKs correspond to A_{on} and A_{off} , respectively. The upstream proteins correspond to the stimulus s' , and the Raf on the upstream pathway affects the phosphorylated ERK. **b** Typical behavior of the phosphorylated ERK fraction P_1 in the activation and inactivation processes. The time t_{ini} (t_{peak}) indicates the beginning of the activation (inactivation), and the time t_{peak} (t_{fin}) indicates the end of the activation (inactivation). **c** Schematic of the manifold in information geometry and the intrinsic speed ds/dt on this manifold. The activation and inactivation processes give at least two peaks in the time series of ds^2/dt^2 , because $ds^2/dt^2 = 0$ at times t_{ini} , t_{peak} , and t_{fin} .

193 during the process from time t_0 to t_1 . The action \mathcal{C} quan-215
 194 tifies the thermodynamic cost of the process because the ac-216
 195 tion $\mathcal{C} \simeq \sigma|_{t=t_0} / (4R[A_{tot}])$ is approximately proportional to217
 196 the entropy production rate at time t_0 under near-equilibrium218
 197 condition. Even for a system far from equilibrium, the action219
 198 \mathcal{C} can be interpreted as the thermodynamic cost in terms of
 199 the fluctuation-response ratio in Eq. (3) and becomes large if
 200 the observable change speed $|d_t \langle f \rangle_t|$ is relatively larger than
 201 its fluctuation $\sqrt{\text{Var}[f]_t}$ during the process. The length \mathcal{L} is
 202 given by twice the Bhattacharyya angle, which is a measure224
 203 of a difference between two concentration fractions at time t_0 225
 204 and time t_1 . The mean velocity \mathcal{V} quantifies the speed of the
 205 concentration fraction change during the process. In informa-227
 206 tion geometry, \mathcal{L} is regarded as the arc length of a circle in
 207 $2\sqrt{P_i}$ coordinate, and ds/dt is the intrinsic speed on this cir-229
 208 cle (see also Fig. 1c). From the Cauchy-Schwarz inequality230
 209 we obtain the thermodynamic speed limit [8]

$$\mathcal{L}^2 \leq 2\mathcal{C}(t_1 - t_0), \quad (7)$$

210 which is a trade-off relation between the thermodynamic cost
 211 \mathcal{C} and the transition time $t_1 - t_0$ during the process. To quan-
 212 tify how much the thermodynamic cost converts into the con-
 213 centration fraction change speed, we can consider the speed237
 214 limit's efficiency [8]

$$\eta = \frac{\mathcal{L}^2}{2(t_1 - t_0)\mathcal{C}} = \frac{\mathcal{V}\mathcal{L}}{2\mathcal{C}}. \quad (8)$$

The efficiency η satisfies $0 \leq \eta \leq 1$, and $\eta = 1$ ($\eta = 0$)
 implies that this conversion is most efficient (inefficient). The
 efficiency becomes higher if the intrinsic speed is close to con-
 stant because $\eta = 1$ if and only if the intrinsic speed ds/dt is
 constant regardless of time, $(d/dt)|ds^2/dt^2| = 0$.

We experimentally measured the phosphorylated ERK frac-
 tion in living NRK-52E cells with the FRET-based ERK
 biosensor, the EKAREV-NLS (Fig. 2a) [41]. By compar-
 ing the fluorescence ratio of cells with the phosphorylated
 ERK fraction obtained from the western blotting (Fig. 2b),
 we quantified P_1 and the square of the intrinsic speed ds^2/dt^2
 for the ERK activation ($p = a$) and inactivation ($p = i$) pro-
 cesses under the condition of different cell densities: 2.0×10^3
 cells/cm² (low, $d = L$), 2.0×10^4 cells/cm² (medium, $d = M$),
 and 2.0×10^5 cells/cm² (high, $d = H$), where the indices
 $p \in \{a, i\}$ and $d \in \{L, M, H\}$ regard the process and cell
 density, respectively. The pulses of the ERK activation were
 observed under these conditions (Fig. 2c and Supplementary
 Video 1), and the behavior of ds^2/dt^2 characterizes these con-
 ditions p and d (Fig. 2d). It reveals thermodynamic differ-
 ences of the intracellular ERK activation under these condi-
 tions.

The information-geometric quantities $\{\mathcal{C}, \mathcal{L}, \mathcal{V}\}_d^p$ also dif-
 ferentiate these conditions (Fig. 3 and Extended Data Table
 2). Firstly, we discuss the histogram of the action. The mean
 value of the action $\overline{\mathcal{C}}_d^p$ becomes larger as cell density increases
 $\overline{\mathcal{C}}_H^p > \overline{\mathcal{C}}_M^p > \overline{\mathcal{C}}_L^p$ for both $p = a$ and $p = i$. It reflects the

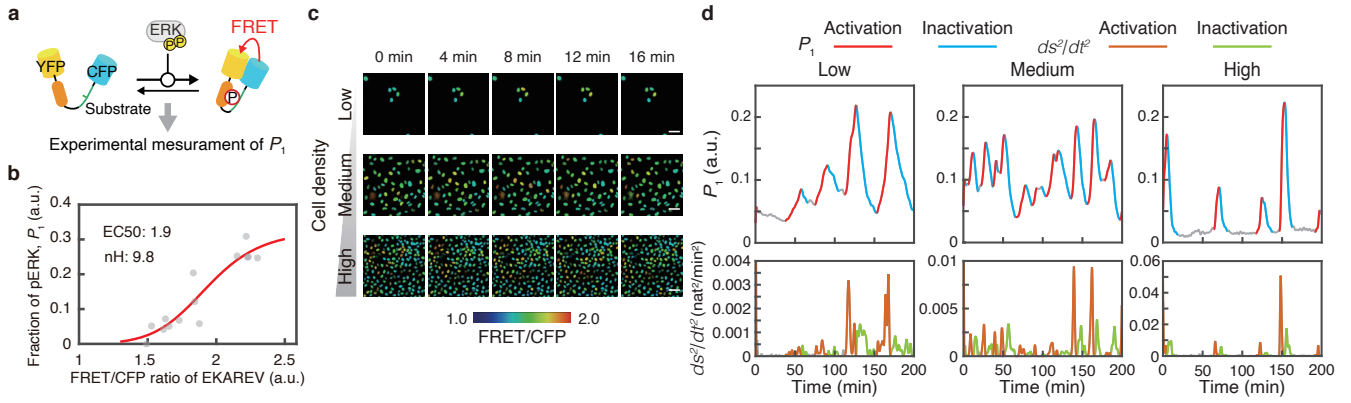


Fig. 2: The dynamics of the ERK phosphorylation under the conditions of different cell densities. **a** Schematic of the FRET-based ERK sensor. The phosphorylated ERK fraction P_1 can be measured from this FRET signal. **b** The relation between the FRET/CFP ratios of the EKAREV-NLS and the phosphorylated ERK fraction P_1 . The red line indicates the fitted curve of the Hill equation. **c** Representative images of the phosphorylated ERK under the conditions of low, medium, and high cell densities. Scale bars indicate $50 \mu\text{m}$. **d** Representative examples of the ERK phosphorylation dynamics under low (left), medium (middle), and high (right) cell densities. The unit (a.u.) indicates the arbitrary unit, and the unit (nat) indicates the natural unit of information.

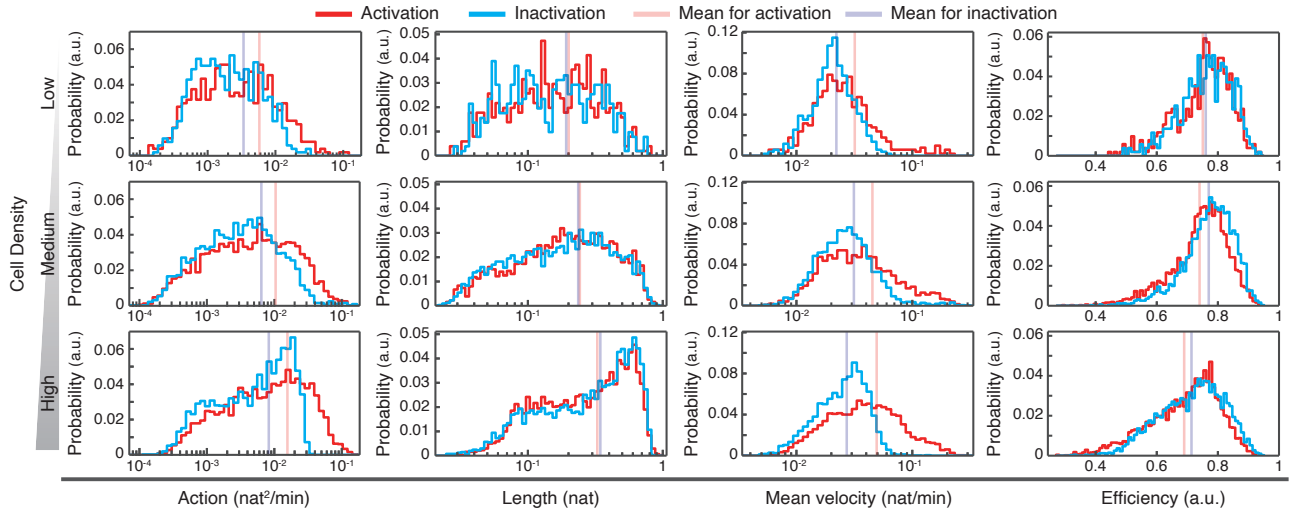


Fig. 3: The histograms of the action \mathcal{C} , length \mathcal{L} , mean velocity \mathcal{V} , and efficiency η under the conditions of different cell densities. The sample size, mean values, variances, and results of statistical tests are listed in Extended Data Table 1, 2.

242 fact that the speed under the condition of the high density ap-253
 243 peared faster than the low density. The difference of $\overline{\mathcal{C}}_d^p$ be-254
 244 tween the high (medium) and low densities is at least twice-255
 245 ($\overline{\mathcal{C}}_H^a/\overline{\mathcal{C}}_L^a \simeq 2.7$, $\overline{\mathcal{C}}_H^i/\overline{\mathcal{C}}_L^i \simeq 2.4$). In comparison with the activa-256
 246 tion and inactivation processes, $\overline{\mathcal{C}}_d^a$ is approximately twice as-257
 247 much as $\overline{\mathcal{C}}_d^i$, and the distributions for the activation have longer-258
 248 tails than the inactivation. Because the action is a measure of-259
 249 the thermodynamic cost, these results suggest that the activa-260
 250 tion's thermodynamic cost is larger than the inactivation's one-261
 251 and becomes larger as cell density increases. Secondly, we-262
 252 discuss the histogram of the length. While the length does not-263

distinguish the activation process from the inactivation pro-
 cess, the mean value of the length $\overline{\mathcal{L}}_d^p$ differentiates the cell
 densities. It reflects the fact that the peak of the spike be-
 comes higher as the cell density increases. Finally, we discuss
 the histogram of the mean velocity. The mean value of the
 mean velocity for the activation $\overline{\mathcal{V}}_d^a$ is larger than the inactivation
 $\overline{\mathcal{V}}_d^i$. It shows that the speed of the activation is faster than
 the inactivation.

From these information-geometric quantities $\{\mathcal{C}, \mathcal{L}, \mathcal{V}\}_d^p$,
 we obtained the speed limit's efficiency $\eta_d^p = \mathcal{V}_d^p \mathcal{L}_d^p / (2\mathcal{C}_d^p)$
 (Fig. 3 right column). The mean value of the speed limit's

264 efficiency is almost $\overline{\eta_d^p} \simeq 0.7$ under these conditions, and the 313
 265 distribution of η_H^p shifted to lower than those of η_L^p and η_M^p 314
 266 (see also Extended Data Table 2). The efficiencies range be- 315
 267 tween $\eta_d^p = 0.4$ and $\eta_d^p = 0.9$, and the distributions' shapes 316
 268 are biased to the higher efficiency. We can detect that the ac- 317
 269 tivation process is less efficient than the inactivation process 318
 270 $\eta_d^a < \eta_d^i$. We also find that the efficiency becomes worse in 319
 271 the higher cell density $\eta_H^p < \eta_L^p$. These results indicate that 320
 272 the process is accelerated under the higher cell density, and 321
 273 the activation process is also more accelerated than the inac- 322
 274 tivation process by the thermodynamic cost. This idea is sup- 323
 275 ported by the histogram of $|d/dt(ds^2/dt^2)|$ (Extended Data 324
 276 Fig. 1), which becomes zero when $\eta = 1$. The mean values 325
 277 of $|d/dt(ds^2/dt^2)|$ for the activation and the high cell density 326
 278 are larger than that for the inactivation and the low cell den- 327
 279 sity, respectively (Extended Data Table. 2). The scatter plot 328
 280 (Extended Data Fig. 2, see also Extended Data Table 4) sug- 329
 281 gests no correlation between η_d^p and $\{C, V\}_d^p$, while V and C 330
 282 seem to have a correlation. Because cell density modulates the 331
 283 ERK activation's excitability through both changes in basal 332
 284 and peak levels of the ERK phosphorylation [37], the cellular 333
 285 density could affect the efficiency of the pulsatile phosphory- 334
 286 lation and the thermodynamic cost.

287 We confirm that these information-geometric quantities 335
 288 show the thermodynamic properties of the ERK phospho- 336
 289 rylation by comparing the Raf inhibitor addition situation. 337
 290 The pulsatile dynamics of the ERK activation is generated by 338
 291 stochastic noise from the Raf and feedback loops [37, 39], and 339
 292 the Gibbs free energy difference of the ERK phosphorylation 340
 293 is induced by stimulus s' from the upstream pathway, includ- 341
 294 ing the Raf [39, 40]. Thus, the Raf inhibitor addition reduces 342
 295 the Gibbs free energy change of the ERK phosphorylation and 343
 296 these information-geometric quantities. To ensure these rela- 344
 297 tionships, we measured the ERK phosphorylation dynamics 345
 298 under the Raf inhibitor (SB590885) addition and compared 346
 299 its dynamics with the original dynamics before adding the Raf 347
 300 inhibitor (Fig. 4). Of note, it is well-known that a low dose of 348
 301 the Raf inhibitor could paradoxically activate the ERK signal- 349
 302 ing through the Raf dimerization [42–44]. The condition of 350
 303 the cell density is medium in this experiment. The applica- 351
 304 tion of a low dose (100 nM) of the Raf inhibitor immediately 352
 305 activated the ERK, and the ERK activity demonstrated slower 353
 306 dynamics than that before the Raf inhibitor treatment and after 354
 307 the activation [37] (Fig. 4a and Supplementary Video 2). This 355
 308 result implies that the thermodynamic cost of the ERK phos- 356
 309 phorylation is immediately increased when adding the Raf in- 357
 310 hibitor. After the dynamics of the relaxation on the upstream 358
 311 pathways, the Raf inhibitor addition generally decreases the 359
 312 thermodynamic cost of the ERK phosphorylation. 360

In Fig. 4b, we show the histograms of these information-geometric quantities and the efficiency $\{C, L, V, \eta\}_d^p$ before ($d' = \text{pre}$) and after ($d' = \text{post}$) the Raf inhibitor addition, where the subscript $d' \in \{\text{pre}, \text{post}\}$ regards the Raf inhibitor addition. The mean value of the action $\overline{C}_{d'}^p$ decreases when the Raf is inhibited $\overline{C}_{\text{pre}}^p > \overline{C}_{\text{post}}^p$, and the mean values differ by one order of magnitude (see also Extended Data Table 3). This result shows the Raf inhibitor addition reduces the thermodynamic cost of the ERK phosphorylation. The mean velocity and length also decrease when the Raf inhibitor is added, $\overline{V}_{\text{pre}}^p > \overline{V}_{\text{post}}^p$, and $\overline{L}_{\text{pre}}^p > \overline{L}_{\text{post}}^p$, while the transition time $t_1 - t_0$ becomes longer by the Raf inhibitor addition (Extended Data Fig. 3 and see also Extended Data Table 3). Surprisingly, the mean value of the efficiency is robust to the Raf inhibitor addition $\overline{\eta}_{\text{pre}}^p \simeq \overline{\eta}_{\text{post}}^p$, while the peak of the histogram can be decreased after adding the Raf inhibitor. Moreover, the efficiency η_d^p seems to have no correlation with $C_{d'}^p$ nor $V_{d'}^p$ (Extended Data Fig. 4 and see also Extended Data Table 4), and this robustness would not come from an artifact correlation between information-geometric quantities. The efficiency compensation of the ERK phosphorylation might exist when the upstream pathways are perturbed by the inhibitor.

In summary, we introduced information-geometric quantities as thermodynamic measures, and evaluated the speed limit's efficiency for the ERK phosphorylation dynamics in living cells at the single-cell level. Our method quantitatively clarifies the amount of information transferred in living systems based on information geometry and the conversion efficiency from the thermodynamic cost to the intrinsic speed, which complements other studies about measurements of informational quantities in biological systems such as the mutual information in signal transduction [46–48] and the Fisher information matrix on molecular networks [49, 50]. Our method is generally applicable to the activation process, and it widely exists in signaling pathways such as the G-protein coupled receptor pathways for sensation [14] and the receptor tyrosine kinase signaling pathways for cell proliferation [45]. For example, the state change from the active state A_{on} to the inactive state A_{off} in the G-protein coupled receptor corresponds to its conformational change by small rearrangements accompanying the ligand-binding. It is interesting to evaluate the speed limit's efficiency for other activation processes on an equal footing with this ERK phosphorylation in living NRK-52E cells. Our approach has great potential for other biological applications, which might clarify an efficient signal transduction mechanism and lead to novel insight into living systems as an information processing unit driven by the thermodynamic cost.

361 [1] Hopfield, J. J. Kinetic proofreading: a new mechanism for- 367
 362 ducing errors in biosynthetic processes requiring high specificity. 368
 363 *Proc. Natl. Acad. Sci. USA* **71**, 4135–4139 (1974). 369
 364 [2] Ninio, J. Kinetic amplification of enzyme discrimination. 370
 365 *Biochimie* **57**, 587–595 (1975). 371
 366 [3] Lan, G., Sartori, P., Neumann, S., Sourjik, V. & Tu, Y. The 372

energy–speed–accuracy trade-off in sensory adaptation. *Nat. Phys.* **8**, 422–428 (2012).
 [4] Mehta, P. & Schwab, D. J. Energetic costs of cellular computation. *Proc. Natl. Acad. Sci. USA* **109**, 17978–17982 (2012).
 [5] Ito, S. & Sagawa, T. Maxwell's demon in biochemical signal transduction with feedback loop. *Nat. Commun.* **6**, 1–6 (2015).

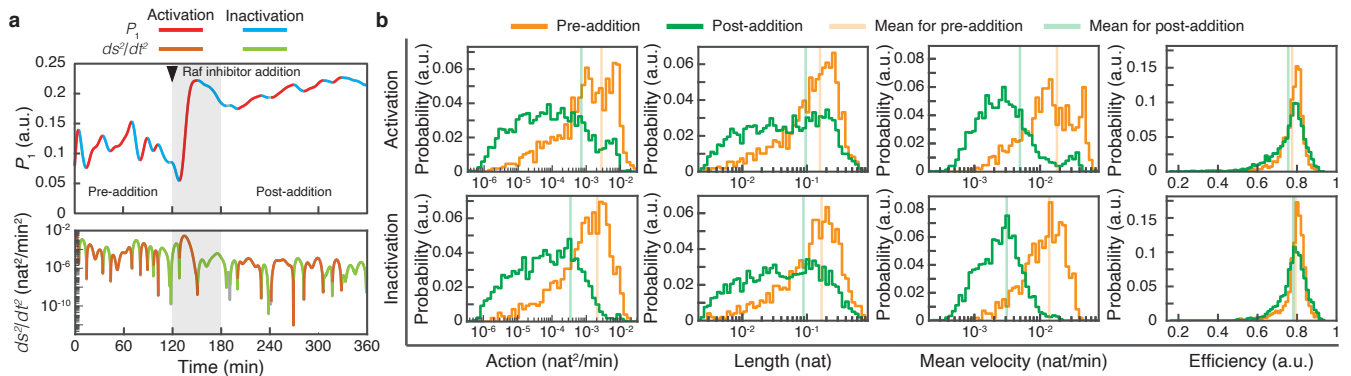


Fig. 4: The dynamics of the ERK phosphorylation under the Raf inhibitor addition. **a** Representative dynamics under the Raf inhibitor addition. The Raf inhibitor (100 nM of SB590885) was applied at 120 min. We set the pre-addition region as the period from 0 min to 120 min, and the post-addition region as the period after 180 min. **b** The histograms of the action \mathcal{C} , length \mathcal{L} , mean velocity \mathcal{V} , and the efficiency η before (pre-addition) and after (post-addition) adding the Raf inhibitor. The sample size, mean values, variances, and results of statistical tests are shown in Extended Data Table 1, 2.

- 373 [6] Parrondo, J. M., Horowitz, J. M. & Sagawa, T. Thermodynamics
374 of information. *Nat. Phys.* **11**, 131–139 (2015). 414
- 375 [7] Crooks, G. E. Measuring thermodynamic length. *Phys. Rev. Lett.*
376 **99**, 100602 (2007). 416
- 377 [8] Ito, S. Stochastic thermodynamic interpretation of information
378 geometry. *Phys. Rev. Lett.* **121**, 030605 (2018). 418
- 379 [9] Ciliberto, S. Experiments in stochastic thermodynamics: Short
380 history and perspectives. *Phys. Rev. X* **7**, 021051 (2017). 420
- 381 [10] Collin, D. et al. Verification of the Crooks fluctuation theorem
382 and recovery of RNA folding free energies. *Nature* **437**, 231–234
383 (2005). 423
- 384 [11] Hayashi, K., Ueno, H., Iino, R. & Noji, H. Fluctuation theorem
385 applied to F_1 -ATPase. *Phys. Rev. Lett.* **104**, 218103 (2010). 425
- 386 [12] Ito, S. & Dechant, A. Stochastic time evolution, information
387 geometry, and the Cramér-Rao bound. *Phys. Rev. X* **10**, 021056
388 (2020). 428
- 389 [13] Yoshimura, K. & Ito, S. Information geometric inequalities
390 of chemical thermodynamics. Preprint at <https://arxiv.org/abs/2005.08444> (2020). 431
- 391 [14] Luttrell, L. M. Reviews in molecular biology and biotechnol-
392 ogy: transmembrane signaling by G protein-coupled receptors.
393 *Mol. Biotechnol.* **39**, 239–264 (2008). 434
- 394 [15] Seifert, U. Stochastic thermodynamics, fluctuation theorems
395 and molecular machines. *Rep. Prog. Phys.* **75**, 126001 (2012). 436
- 396 [16] Rao, R. & Esposito, M. Nonequilibrium thermodynamics of
397 chemical reaction networks: wisdom from stochastic thermody-
398 namics. *Phys. Rev. X* **6**, 041064 (2016). 439
- 399 [17] Ge, H. & Qian, H. Nonequilibrium thermodynamic formalism
400 of nonlinear chemical reaction systems with Waage-Guldberg’s
401 law of mass action. *Chem. Phys.* **472**, 241–248 (2016). 442
- 402 [18] Ito, S. & Sagawa, T. Information thermodynamics on causal
403 networks. *Phys. Rev. Lett.* **111**, 180603 (2013). 444
- 404 [19] Barato, A. C., Hartich, D. & Seifert, U. Efficiency of cellular
405 information processing. *New J. Phys.* **16**, 103024 (2014). 446
- 406 [20] Sartori, P., Granger, L., Lee, C. F. & Horowitz, J. M. Thermo-
407 dynamic costs of information processing in sensory adaptation.
408 *PLoS Comput. Biol.* **10**, e1003974 (2014). 449
- 409 [21] Barato, A. C. & Seifert, U. Thermodynamic uncertainty relation
410 for biomolecular processes. *Phys. Rev. Lett.* **114**, 158101 (2015). 451
- 411 [22] Horowitz, J. M. & Gingrich, T. R. Thermodynamic uncertainty
412 relations constrain non-equilibrium fluctuations. *Nat. Phys.* **16**,
15–20 (2020).
- [23] Shiraishi, N., Funo, K. & Saito, K. Speed limit for classical
stochastic processes. *Phys. Rev. Lett.* **121**, 070601 (2018).
- [24] Ashida, K. & Oka, K. Stochastic thermodynamic limit on *E. coli*
adaptation by information geometric approach. *Biochem. Biophys. Res. Commun.* **508**, 690–694 (2019).
- [25] Dechant, A. & Sakurai, Y. Thermodynamic interpretation
of Wasserstein distance. Preprint at <https://arxiv.org/abs/1912.08405> (2019).
- [26] Gupta, D. & Busiello, D. M. Tighter thermodynamic bound on
speed limit in systems with unidirectional transitions. Preprint at
<https://arxiv.org/abs/2009.11115> (2020).
- [27] Zhang, Z., Guan, S. & Shi, H. Information geometry in the pop-
ulation dynamics of bacteria. *J. Stat. Mech.* **2020**, 073501 (2020).
- [28] Falasco, G. & Esposito, M. Dissipation-time uncertainty rela-
tion. *Phys. Rev. Lett.* **125**, 120604 (2020).
- [29] Nicholson, S. B., Garcia-Pintos, L. P., del Campo, A. & Green, J. R.
Time-information uncertainty relations in thermodynamics. *Nat. Phys.* (2020).
- [30] Dechant, A. Multidimensional thermodynamic uncertainty rela-
tions. *J. Phys. A* **52**, 035001 (2018).
- [31] Amari, S. *Information Geometry and Its Applications*. (Springer, Japan, 2016).
- [32] Ruppeiner, G. Riemannian geometry in thermodynamic fluctu-
ation theory. *Rev. Mod. Phys.* **67**, 605 (1995).
- [33] Ito, S., Oizumi, M. & Amari, S. Unified framework for the en-
tropy production and the stochastic interaction based on infor-
mation geometry. *Phys. Rev. Research* **2**, 033048 (2020).
- [34] Pietzonka, P., Ritort, F. & Seifert, U. Finite-time generaliza-
tion of the thermodynamic uncertainty relation. *Phys. Rev. E* **96**,
012101 (2017).
- [35] Paneru, G., Dutta, S., Tlusty, T. & Pak, H. K. Reaching and
violating thermodynamic uncertainty bounds in information en-
gines. *Phys. Rev. E* **102**, 032126 (2020).
- [36] Albeck, J. G., Mills, G. B. & Brugge, J. S. Frequency-
modulated pulses of ERK activity transmit quantitative prolifer-
ation signals. *Mol. Cell* **49**, 249–261 (2013).
- [37] Aoki, K. et al. Stochastic ERK activation induced by noise and
cell-to-cell propagation regulates cell density-dependent prolifer-

- 453 eration. *Mol. Cell* **52**, 529–540 (2013).
- 454 [38] Yang, J. M. et al. Integrating chemical and mechanical signals through dynamic coupling between cellular protrusions and
455 pulsed ERK activation. *Nat. Commun.* **9**, 4673 (2018).
- 456 [39] Lavoie, H., Gagnon, J. & Therrien, M. ERK signalling: a master
457 regulator of cell behaviour, life and fate. *Nat. Rev. Mol. Cell*
458 *Biol.* **21**, 607–632 (2020).
- 459 [40] Knowles, J. R. Enzyme-catalyzed phosphoryl transfer reactions. *Annu. Rev. Biochem.* **49**, 877–919 (1980).
- 460 [41] Komatsu, N. et al. Development of an optimized backbone of
461 FRET biosensors for kinases and GTPases. *Mol. Biol. Cell* **22**,
462 4647–4656 (2011).
- 463 [42] Hatzivassiliou, G. et al. RAF inhibitors prime wild-type RAF
464 to activate the MAPK pathway and enhance growth. *Nature* **464**,
465 431–435 (2010).
- 466 [43] Heidorn, S. J. et al. Kinase-dead BRAF and oncogenic RAS
467 cooperate to drive tumor progression through CRAF. *Cell* **140**,
468 209–221 (2010).
- 469 [44] Poulikakos, P. I. et al. RAF inhibitor resistance is mediated by
470 dimerization of aberrantly spliced BRAF (V600E). *Nature* **480**,
471 387–390 (2011).
- 472 [45] Lemmon, M. A. & Schlessinger, J. Cell signaling by receptor
473 tyrosine kinases. *Cell* **141**, 1117–1134 (2010).
- 474 [46] Mehta, P., Goyal, S., Long, T., Bassler, B. L. & Wingreen, N. S.
475 Information processing and signal integration in bacterial quorum
476 sensing. *Mol. Syst. Biol.* **5**, 325 (2009).
- 477 [47] Uda, S. et al. Robustness and compensation of information
478 transmission of signaling pathways. *Science* **341**, 558–561
479 (2013).
- 480 [48] Selimkhanov, J. et al. Accurate information transmission
481 through dynamic biochemical signaling networks. *Science* **346**,
482 1370–1373 (2014).
- 483 [49] Machta, B. B., Chachra, R., Transtrum, M. K. & Sethna, J.
484 P. Parameter space compression underlies emergent theories and
485 predictive models. *Science* **342**, 604–607 (2013).
- 486 [50] Singh, V. & Nemenman, I. Universal properties of concentration
487 sensing in large ligand-receptor networks. *Phys. Rev. Lett.*
488 **124**, 028101 (2020).
- 489
490

Measurement of the phosphorylated ERK fraction

We measured the ERK phosphorylation, as previously described [51]. The EKAREV-NLS stable-expression NRK-52E cell lines (NRK-52E/ERKAREV-NLS cells) [37], were used, and the EKAREV-NLS is the genetically encoded ERK sensor used in Komatsu *et al.*, 2011 [41].

The NRK-52E/EKAREV-NLS cells were maintained with the Dulbecco's Modified Eagle Medium (DMEM; ThermoFisher), 10 % Fetal bovine serum (FBS; Sigma), and 10 μ g/mL Blasticidin S (Invitrogen). The cells were seeded at a specific concentration (Low: 2.0×10^3 cells/cm², Medium: 2.0×10^4 cells/cm², High: 2.0×10^5 cells/cm²) on glass bottom dishes (IWAKI). One day after the seeding, the time-lapse imaging was performed. The culture media was replaced with the FluoroBrite (ThermoFisher), 5 % FBS (Sigma), and 1 \times Glutamax (ThermoFisher) 3–6 hours before starting the time-lapse imaging. We used an inverted microscope (IX81; Olympus) equipped with a CCD camera (CoolSNAP K4; Roper Scientific) and an excitation light source (Spectra-X light engine; Lumencor). Optical filters were as follows: an FF01-438/24 excitation filter (Semrock), an XF2034 (455DRLP) dichroic mirror (Omega Optical), and two emission filters (FF01-483/32 for CFP and FF01-542/27 for YFP (Semrock)). Images were acquired every 20 sec (the exposure time was 100 ms) with binning 8 \times 8 on MetaMorph software (Universal Imaging) with an IX2-ZDC laser-based autofocusing system (Olympus). A \times 20 lens (UPLSAPO 20X; Olympus, numerical aperture: 0.75) was used. The temperature and CO₂ concentration were maintained at 37°C and 5 % during the imaging with a stage top incubator (Tokaihit). For the Raf inhibitor experiment, the experiment was performed under the same condition as the medium cell density condition. We applied SB590885 (Selleck Chemicals) (a final concentration is 100 nM) 2 hours after the imaging initiation. The numbers of trials for each experimental condition are two.

We used the same relation between the FRET/CFP ratios of the EKAREV-NLS and the phosphorylated ERK fraction (pTpY-ERK2) from the western blotting in Fig. 2b as described previously [37]. In brief, the phosphorylated ERK fraction was quantified by the Phos-tag western blotting [52] in HeLa cells stimulated with different concentrations of 12-O-Tetradecanoylphorbol 13-acetate (TPA; Sigma) for 30 min to induce the ERK phosphorylation. Under the same condition, HeLa cells stably expressing EKAREV-NLS were imaged, followed by the quantification of the average FRET/CFP ratios. Finally, the FRET/CFP ratios were plotted as a function of the phosphorylated ERK fraction with the fitted curve of the Hill equation shown in Fig. 2b by the Solver Add-in in Excel (Microsoft).

For the imaging analysis, Fiji was used. The background was subtracted by the Subtract Background Tool, and after that, the nuclei were tracked with a custom-made tracking program. Only the cells which were tracked over the entire images were used for calculation of information-geometric quantities. The phosphorylated ERK fraction was calculated based on the FRET/CFP ratios with the Hill equation shown in Fig. 2b.

For analysis of the time-series phosphorylated ERK fractions, MATLAB 2019b (MathWorks) was used. The low-pass filter, whose cutoff frequency is 0.005 Hz, was used for the cell density experiment data with the designfilt function in the Signal Processing Toolbox to reduce the noise. The low-pass filter, whose cutoff frequency is 1/1200 Hz, was used for the Raf inhibitor addition experiment data to detect the slower dynamics after the Raf inhibitor addition. We identified the activation and inactivation processes from the signs of the first and second derivatives. The first derivatives were numerically calculated using two data points of the phosphorylated fraction, and the second derivatives were numerically calculated using two data points of the first derivatives. We only calculated information-geometric quantities when the phosphorylated ERK fractions between maximum and minimum of the process over 0.01 for the density-experiment data and 0.001 for the Raf inhibitor addition experiment data. The square of an intrinsic speed ds^2/dt^2 was numerically calculated using two-points of the phosphorylated ERK fraction time series. The action \mathcal{C} , length \mathcal{L} , mean velocity \mathcal{V} , and efficiency η were calculated using ds^2/dt^2 according to the definitions. We used the set of time series for each cell in two trials for each experimental condition to make histograms.

For the statistical analysis, R (version 3.6.3; R project) was used. The Brunner-Munzel test was performed with the brunnermunzel.test function in the brunnermunzel library (version 1.4.1). The two-sample Kolmogorov-Smirnov test was performed with the ks.test function in the stats library (version 3.6.3). The Pearson correlation coefficients were calculated and tested by the cor.test function in the stats library (version 3.6.3). The Holm method was used to control the family-wise error rates with the p.adjust function in the stats library (version 3.6.3). The sample numbers are shown in Extended Data Table 1.

DATA AVAILABILITY

The data sets generated and analyzed during the current study are available from the corresponding author on reasonable request.

CODE AVAILABILITY

The source codes used in the current study are available from the corresponding author on reasonable request.

ACKNOWLEDGEMENTS

592

593 S. I. is supported by JSPS KAKENHI Grants No. 608
594 JP19H05796, and JST Presto Grant No. JP18070368, Japan.
595 Kazuhiro Aoki is supported by JSPS KAKENHI Grants No.
596 JP19H05798. S. I. and Keita Ashida thank Kohei Yoshimura
597 for discussions of chemical thermodynamics, S. I. thanks Keita
598 Kamino for the discussion of experimental difficulties in mea-
599 surement of information quantity of living cells, and Kazuhiro
600 Aoki thanks Yohei Kondo for helpful discussions of thermo-
601 dynamics. S. I. also thanks Kiyoshi Kanazawa for careful
602 reading of this manuscript.

606 experiments. Keita Ashida analyzed the data. All authors dis-
607 cussed the analytical results of the experiment and wrote the
608 paper.

AUTHOR CONTRIBUTIONS

603

604 S. I. proposed the main method based on information ge-
605 ometry and designed the research. Kazuhiro Aoki performed

COMPETING INTERESTS STATEMENT

609

The authors declare no competing interests.

-
- 611 [51] Aoki, K. & Matsuda, M. Visualization of small GTPase activity
612 with fluorescence resonance energy transfer-based biosensors.
613 *Nat. Protoc.* **4**, 1623–1631 (2009).
614 [52] Kinoshita, E., Kinoshita-Kikuta, E., Takiyama, K. & Koike, T.
615 Phosphate-binding tag, a new Tool to visualize phosphorylated
616 proteins. *Mol. Cell. Proteom.* **5**, 749–757 (2006).

Figures

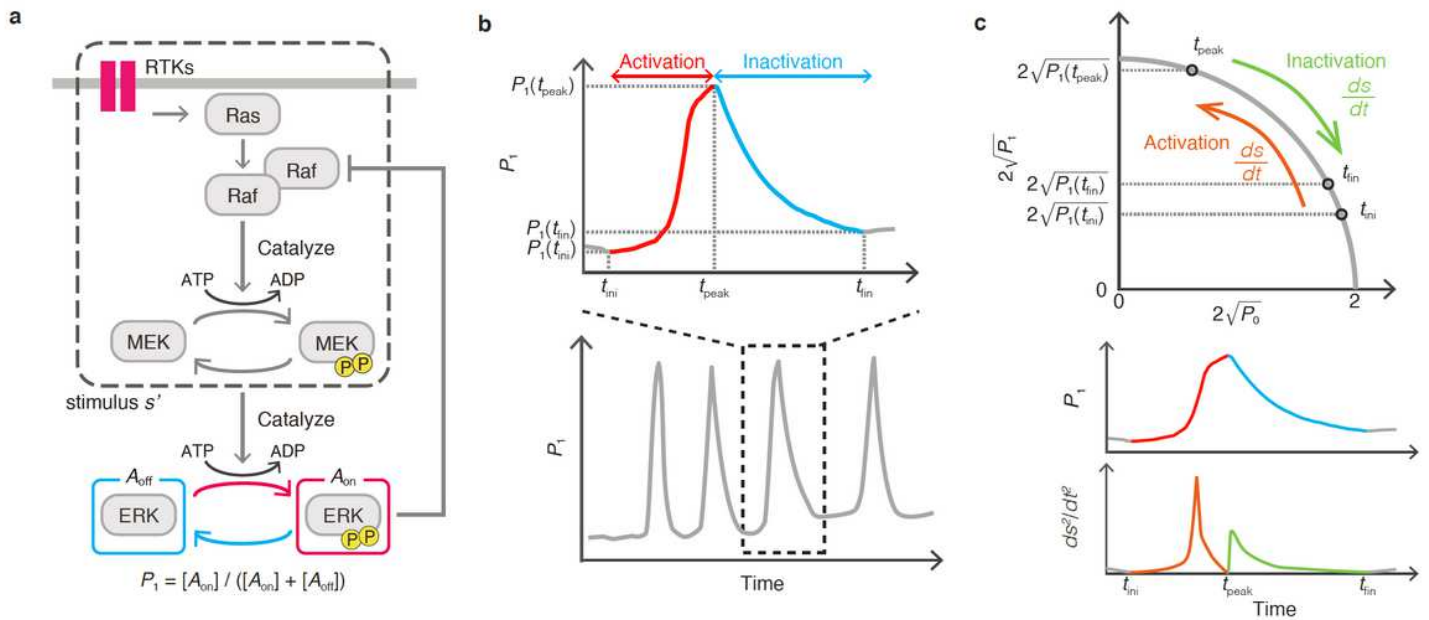


Figure 1

Schematic of the ERK phosphorylation, the time series of the phosphorylated ERK fraction P_1 , and the square of the intrinsic speed ds^2/dt^2 . a The Raf-MEK-ERK MAP pathway as an example of switching dynamics between the active state A_{on} and the inactive state A_{off} . The phosphorylated and nonphosphorylated ERKs correspond to A_{on} and A_{off} , respectively. The upstream proteins correspond to the stimulus s' , and the Raf on the upstream pathway affects the phosphorylated ERK. b Typical behavior of the phosphorylated ERK fraction P_1 in the activation and inactivation processes. The time t_{ini} (t_{peak}) indicates the beginning of the activation (inactivation), and the time t_{peak} (t_{fin}) indicates the end of the activation (inactivation). c Schematic of the manifold in information geometry and the intrinsic speed ds/dt on this manifold. The activation and inactivation processes give at least two peaks in the time series of ds^2/dt^2 , because $ds^2/dt^2 = 0$ at times t_{ini} , t_{peak} , and t_{fin} .

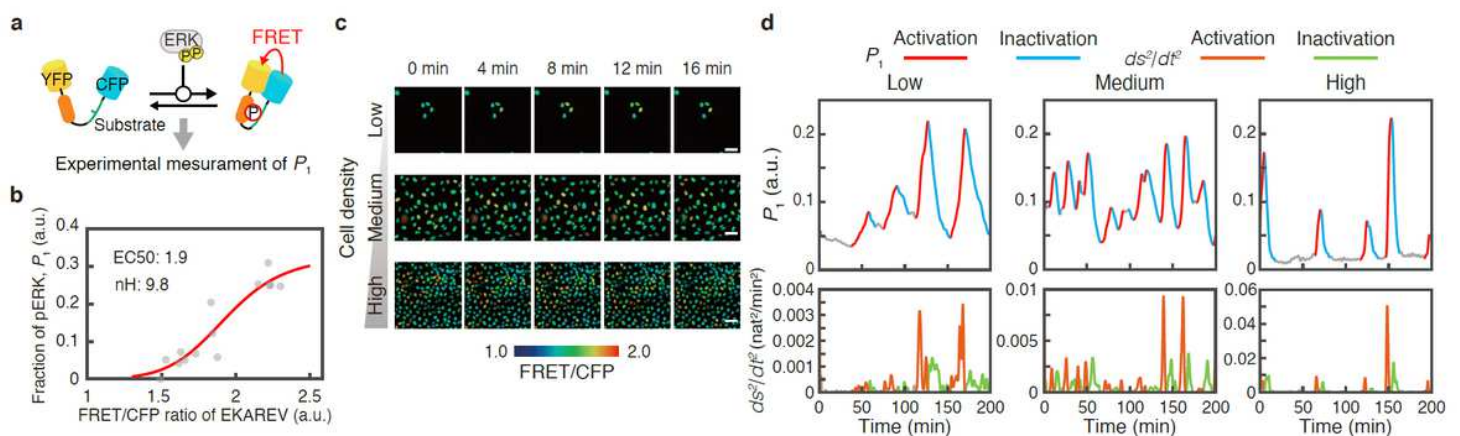


Figure 2

The dynamics of the ERK phosphorylation under the conditions of different cell densities. a Schematic of the FRET-based ERK sensor. The phosphorylated ERK fraction P1 can be measured from this FRET signal. b The relation between the FRET/CFP ratios of the EKAREV-NLS and the phosphorylated ERK fraction P1. The red line indicates the fitted curve of the Hill equation. c Representative images of the phosphorylated ERK under the conditions of low, medium, and high cell densities. Scale bars indicate 50 μm . d Representative examples of the ERK phosphorylation dynamics under low (left), medium (middle), and high (right) cell densities. The unit (a.u.) indicates the arbitrary unit, and the unit (nat) indicates the natural unit of information.

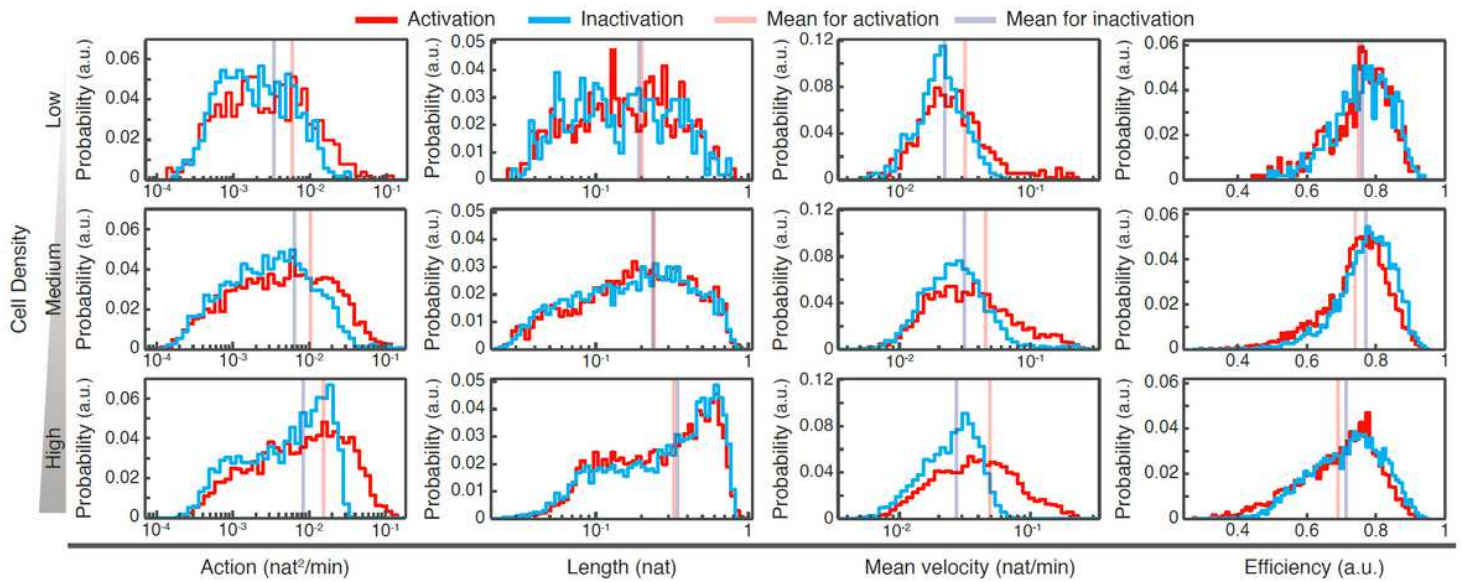


Figure 3

The histograms of the action C , length L , mean velocity V , and efficiency η under the conditions of different cell densities. The sample size, mean values, variances, and results of statistical tests are listed in Extended Data Table 1, 2.

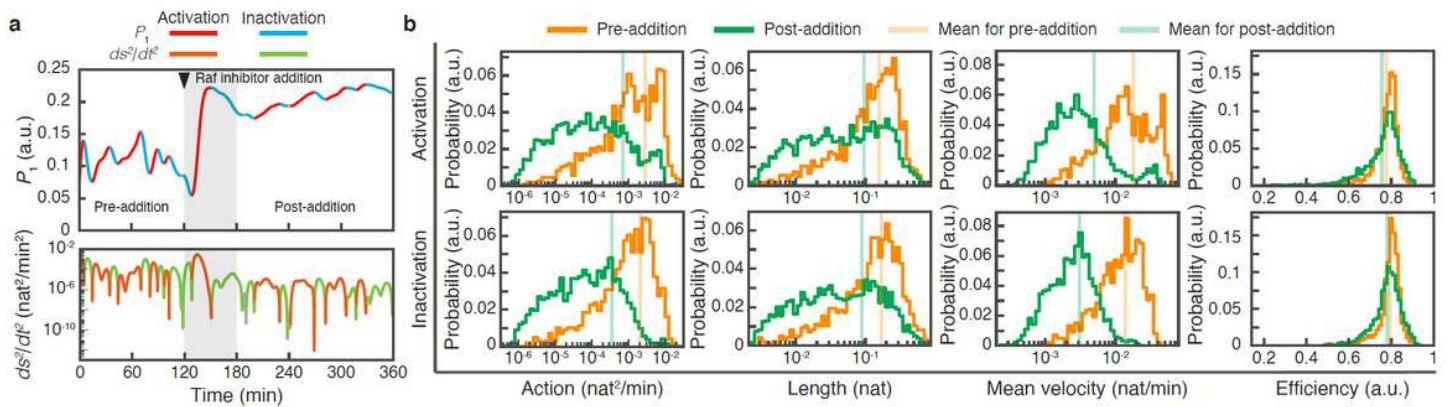


Figure 4

The dynamics of the ERK phosphorylation under the Raf inhibitor addition. a Representative dynamics under the Raf inhibitor addition. The Raf inhibitor (100 nM of SB590885) was applied at 120 min. We set the pre-addition region as the period from 0 min to 120 min, and the post-addition region as the period after 180 min. b The histograms of the action C, length L, mean velocity V, and the efficiency η before (pre-addition) and after (post-addition) adding the Raf inhibitor. The sample size, mean values, variances, and results of statistical tests are shown in Extended Data Table 1, 2.

Supplementary Files

This is a list of supplementary files associated with this preprint. Click to download.

- [VideoS1.mov](#)
- [VideoS2.mov](#)
- [supplements.pdf](#)